catalysts

MDPI

Article

A Single-Atom Au Catalyst Boosts High-Efficiency Electrochemical Seawater Oxidation

Qihao Sha [1,†], Jian Shen [2,3,†], Guotao Yang [1], Tianshui Li [1], Wei Liu [1], Yun Kuang [1,4,*] and Xiaoming Sun [1]

[1] State Key Laboratory of Chemical Resource Engineering, Beijing Advanced Innovation Center for Soft Matter Science and Engineering, College of Chemistry, Beijing University of Chemical Technology, Beijing 100029, China; shaqh@buct.edu.cn (Q.S.); 18754398255@163.com (G.Y.); litianshui@buct.edu.cn (T.L.); liuv@buct.edu.cn (W.L.); sunxm@mail.buct.edu.cn (X.S.)
[2] School of Science, Harbin Institute of Technology, Shenzhen 518055, China; shenjianc@sec.com.cn
[3] Shenzhen Energy Group Co., Ltd., No. 2026 Jintian Rd., Shenzhen 518031, China
[4] Ocean Hydrogen Energy R&D Center, Research Institute of Tsinghua University in Shenzhen, Shenzhen 518057, China
* Correspondence: kuangy@tsinghua-sz.org
† These authors contributed equally to this work.

Abstract: Alkaline seawater electrolysis has garnered significant attention as an efficient, green, and sustainable method for producing green hydrogen in recent years. However, the lack of highly active anodes in seawater electrolysis to prevent chloride oxidation reactions has limited its commercial application. In this study, Au single atoms were deposited on NiCoFeS through the electrochemical deposition method. The optimized catalyst exhibited significantly enhanced activity in seawater electrolyte; the Au@NiCoFeS catalyst achieved a current density of 10 mA/cm^2 with only 183 mV and maintained its performance without degradation for 250 h at a current density of 200 mA/cm^2, with no corrosion observed on either the catalyst or the substrate.

Keywords: seawater splitting; single-atom catalysis; oxygen evolution reaction

Citation: Sha, Q.; Shen, J.; Yang, G.; Li, T.; Liu, W.; Kuang, Y.; Sun, X. A Single-Atom Au Catalyst Boosts High-Efficiency Electrochemical Seawater Oxidation. *Catalysts* **2024**, *14*, 348. https://doi.org/10.3390/catal14060348

Academic Editor: Yurii V. Geletii

Received: 14 April 2024
Revised: 17 May 2024
Accepted: 20 May 2024
Published: 29 May 2024

1. Introduction

Electrolytic hydrogen production from seawater offers an economical, sustainable, and efficient strategy for renewable hydrogen generation [1–5]. However, the abundant presence of Cl^- ions in seawater poses a challenge to the anodic catalysts [6–10]. Effective and sustainable seawater electrolysis requires highly active and stable anodic catalysts capable of maintaining an overpotential for the oxygen evolution reaction (OER) consistently below 480 mV to prevent chloride oxidation reactions (CIORs) [11]. Previous studies have shown that Ni-, Co-, and Fe-based phosphides [12], sulfides [2,13,14], selenides [15], nitrides [6,16], and hydroxides [17–20] exhibit excellent stability in seawater environments, but their activity needs further enhancement.

Single-atom catalysts, highly dispersing isolated atoms on the surface of a carrier as catalytic centers, have demonstrated outstanding catalytic activity, selectivity, and maximal atomic utilization, making them widely applicable in electrocatalysis [21–25]. Individual atoms can form strong chemical bonds with non-metallic elements such as N, P, and S, optimizing the electronic configuration of active sites to achieve enhanced electrocatalytic activity. Recent reports have demonstrated that Ir single atoms loaded on CoFe-LDH via impregnation exhibit excellent OER activity and selectivity in both alkaline and seawater environments [17]. However, the impregnation method for preparing single-atom catalysts has strict synthesis requirements, and the preparation process may lead to the migration and aggregation of metal atoms. Other methods for preparing single-atom catalysts, such as co-precipitation, atomic layer deposition, high-temperature atomic trapping, ion exchange, and ligand-assisted methods, have lower efficiency.

In this study, we employed self-supported NiCoFeS as a carrier and used cyclic voltammetry to load single-atom Au onto NiCoFeS nanosheets as alkaline seawater electrolysis catalysts. HAADF-STEM confirmed the existence of Au in a single-atom form. The Au@NiCoFeS catalyst exhibited excellent electrochemical activity and stability in both alkaline and seawater electrolytes, requiring only 201 mV and 183 mV overpotentials to achieve a current density of 10 mA/cm^2, respectively. Moreover, it maintained stable operation at a current density of 200 mA/cm^2 for 250 h in both alkaline and seawater electrolytes. The loading of Au single atoms effectively increased the electrochemical specific surface area of the catalyst and reduced the charge transfer resistance. Additionally, its activity in seawater electrolyte even surpassed that in alkaline electrolyte, which may be attributed to the in situ regulation of the Au coordination environment by the abundant Cl^- ions in seawater.

2. Results

The Au@NiCoFeS catalyst was prepared using a two-step hydrothermal method combined with electrodeposition (Figure 1a). Scanning electron microscope (SEM) images of Ni foam, NiCoFeS, and Au@NiCoFeS are shown in Figure 1b and Supplementary Figure S1. The images indicate that NiCoFeS exhibits a nanosheet array structure [26], and its larger specific surface area provides good support for loading single Au atoms [25]. The SEM image of Au@NiCoFeS indicates that the morphology of the catalyst remains unchanged after loading single Au atoms. Furthermore, EDS elemental mapping of Au@NiCoFeS (Supplementary Figure S2) confirms the homogeneous distribution of the elements. Transmission electron microscopy (TEM) images of Au@NiCoFeS (Figure 1c and Supplementary Figure S3) corroborate the SEM images, further confirming the nanosheet structure of the material with a width of approximately 40 nm. Additionally, no significant clusters or nanoparticles are observed in the TEM images, indicating the uniform dispersion of Au on the substrate. The high-angle annular dark-field scanning transmission electron microscopy (HAADF-STEM) image further demonstrates the uniform dispersion of Au single atoms on the NiCoFeS substrate, with no noticeable clusters or particles (Figure 1d). The XRD patterns of Au@NiCoFeS and NiCoFeS are shown in Supplementary Figure S4. The peaks observed at 38.05° and 50.19° are attributed to the diffraction peaks of Ni_3S_2, while those at 31.35° and 55.37° correspond to Co_3S_4, and the peak at 22.12° is attributed to Fe_9S_{10}. The XRD patterns indicate that the diffraction peaks of Au@NiCoFeS prepared by cyclic voltammetry are consistent with the NiCoFeS substrate. No significant shifts in diffraction peaks are observed, and there are no diffraction peaks corresponding to metallic Au, demonstrating that Au does not form clusters or particles on the substrate.

High-resolution XPS spectra were further employed to investigate the electronic structure and coordination state of Au@NiCoFeS. The Ni 2p XPS spectra (Figure 2a) reveal fitting peaks at 855.68 eV and 873.48 eV, attributed to Ni^{2+} $2p_{3/2}$ and Ni^{2+} $2p_{1/2}$, respectively, which may correspond to the Ni-O species. The fitting peak at 852.98 eV and 871.28 eV corresponded to Ni^0 species, potentially resulting from the reduction of Ni species during the hydrothermal sulfidation process. Peaks at 861.48 eV and 879.58 eV correspond to the satellite peaks of Ni $2p_{3/2}$ and Ni $2p_{1/2}$ [14,16]. Figure 2b shows the Co 2p spectrum, with fitting peaks at 780.95 eV and 796.65 eV corresponding to Co^{2+} $2p_{3/2}$ and Co^{2+} $2p_{1/2}$, which are attributed to Co-O species. Meanwhile, the peaks at 778.38 eV and 793.08 eV are assigned to Co^0 species, while peaks at 786.38 eV and 801.08 eV correspond to the satellite peaks of Co $2p_{3/2}$ and Co $2p_{1/2}$. For the Fe 2p spectra (Figure 2c), the peaks observed at 712.28 eV and 723.68 eV are attributed to Fe^{2+} $2p_{3/2}$ and Fe^{2+} $2p_{1/2}$, respectively, which may correspond to Fe-O bonding. The peaks at 716.28 eV and 725.98 eV are assigned to Fe^{3+} $2p_{3/2}$ and Fe^{3+} $2p_{1/2}$, respectively, potentially corresponding to high-coordination Fe-O species. Peaks at 706.58 eV and 721.48 eV are attributed to Fe^0 species, while the double peaks observed at 719.48 eV and 728.68 eV are assigned to satellite peaks of Fe $2p_{3/2}$ and Fe $2p_{1/2}$, respectively [14]. The S 2p XPS spectrum (Supplementary Figure S5) reveals a fitting peak at 168.18 eV attributed to S=O, indicating oxidation of the catalyst when exposed to air, while peaks at 161.58 eV and 162.98 eV correspond to M-S, demonstrating the presence

of sulfides in the sample [18]. Figure 2d displays the Au 4f XPS spectrum, with fitting peaks at 84.98 eV and 89.28 eV attributed to Au^{+} species [27], potentially corresponding to Au-S and Au-Cl coordination. The peaks observed at 83.88 eV and 87.58 eV are attributed to Au^{0} species, which may result from the lower oxidation state of Au under the electrodeposition loading at the reduction potential; it is possible that Au is dispersed in an alloy-like manner with surrounding metals.

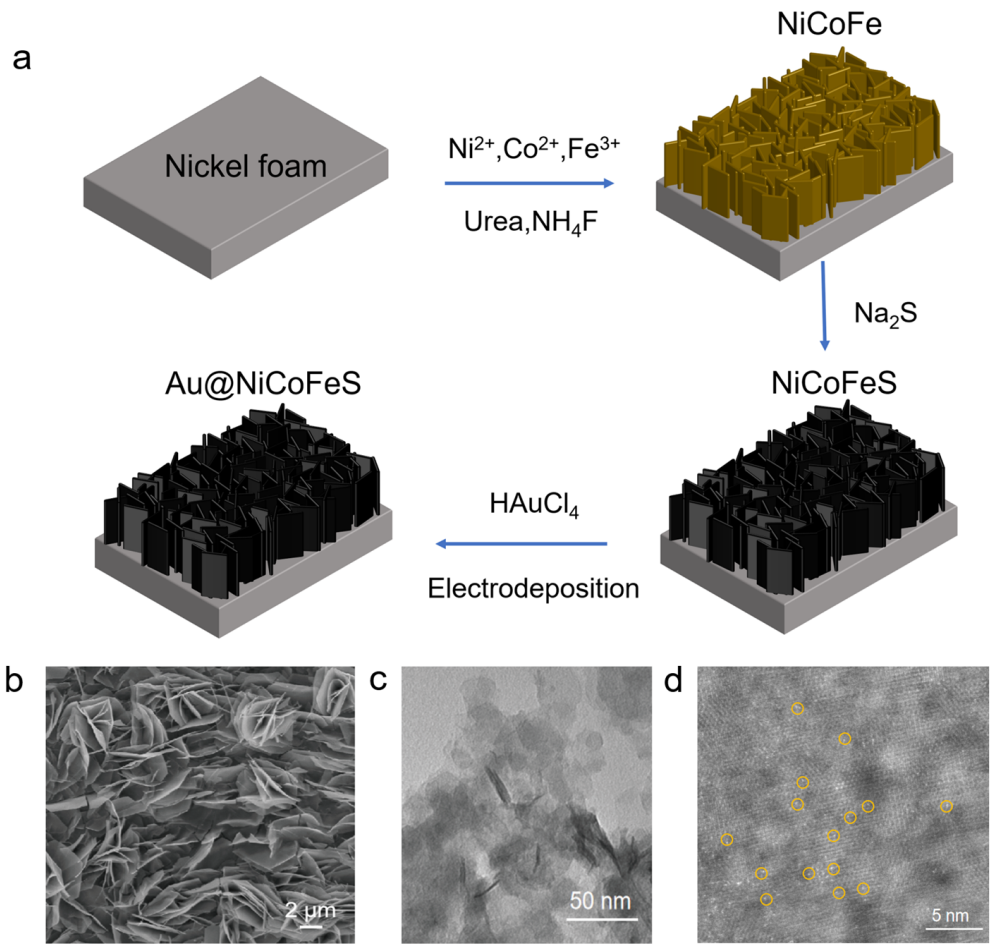

Figure 1. (**a**) Synthesis schematic of Au@NiCoFeS. (**b**) SEM image of Au@NiCoFeS. (**c**) TEM image of Au@NiCoFeS. (**d**) HAADF-STEM image of Au@NiCoFeS.

The OER performance of Au@NiCoFeS was evaluated in 1 M KOH using a conventional three-electrode system. The polarization curves in Figure 3a indicate that Au@NiCoFeS exhibits an overpotential of only 201 mV at a current density of 10 mA/cm^2, which is 21 mV lower than that of NiCoFeS and superior to both NiCoFe (228 mV) and Ni foam (267 mV), demonstrating that the introduction of single-atom Au enhances the electrode's OER activity. Importantly, the OER activity of the Au@NiCoFeS electrode surpasses that of the current commercial catalyst IrO_2 (Figure 3b), which required nearly 240 mV to reach 10 mA/cm^2, highlighting its potential and prospects for scaled-up applications. In industrial applications, electrocatalytic water splitting often requires operation at higher current densities. Therefore, we further investigated the OER activity of the Au@NiCoFeS electrode at a current density of 200 mA/cm^2. Au@NiCoFeS required only 264 mV of overpotential to achieve a current density of 200 mA/cm^2, which outperforms both NiCoFeS (275 mV) and the commercial IrO_2 (366 mV). This indicates that even at high current densities, Au@NiCoFeS maintains excellent activity, demonstrating its potential for efficient hydrogen production. The Tafel slopes of each material are depicted in Figure 3c. The Tafel slope of the Au@NiCoFeS electrode is only 24.2 mV dec^{-1}, lower than that of

NiCoFeS (25.4 mV dec^{-1}) and NiCoFe (33.4 mV dec^{-1}), indicating that the loading of single-atom Au effectively promotes the kinetics of the OER. Additionally, the Nyquist plot in Figure 3d demonstrates that the Au@NiCoFeS electrode exhibits lower charge transfer resistance compared to other electrodes. This suggests that the loading of single-atom Au reduces the resistance of the electrode, thereby enhancing electron transfer kinetics.

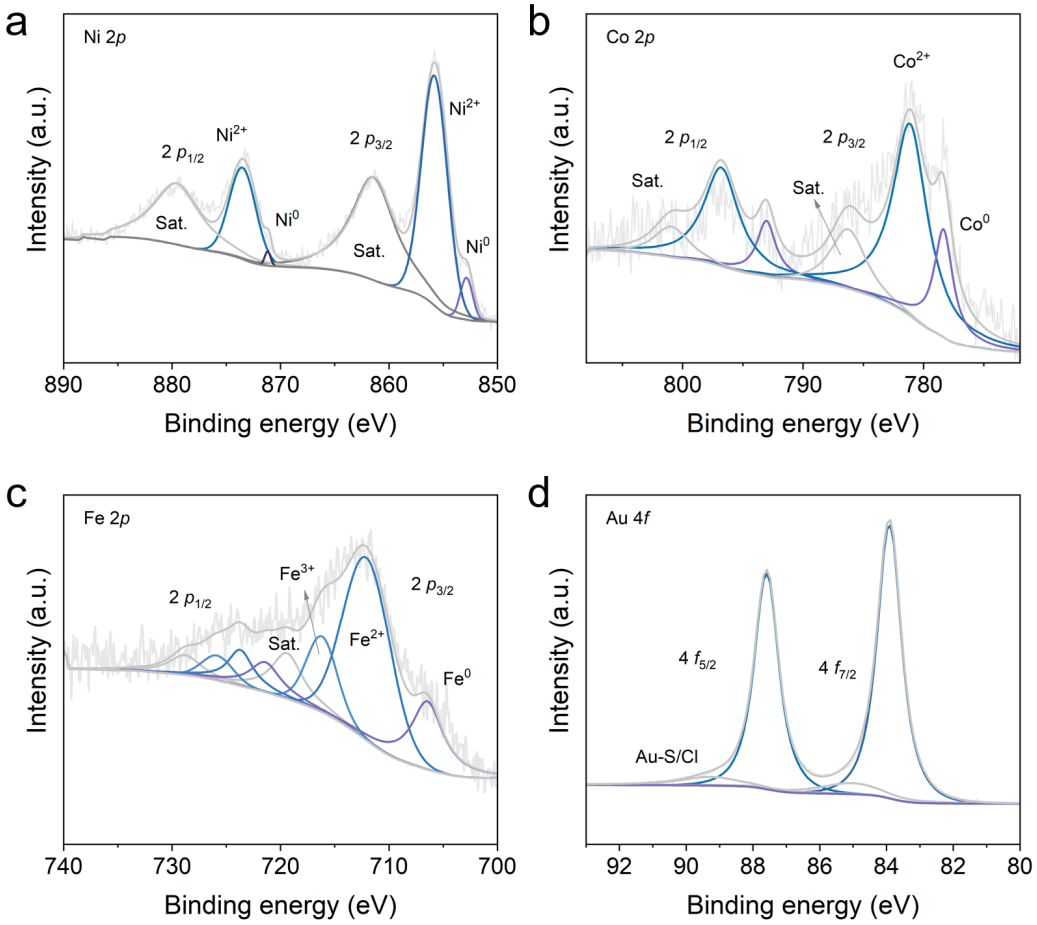

Figure 2. High-resolution XPS spectra of (**a**) Ni 2p, (**b**) Co 2p, (**c**) Fe 2p, and (**d**) Au 4f of Au@NiCoFeS.

Additionally, the deposition of single-atom Au via electrodeposition requires precise control over the deposition cycles and the amount of noble metal to ensure optimal electrocatalytic OER performance. By varying the deposition cycles and the amount of $HAuCl_4 \cdot 4H_2O$ (Figure 3a and Supplementary Figure S6a,b), the OER catalytic performance of Au@NiCoFeS electrodes prepared under different conditions was compared in 1 M KOH electrolyte. The results indicate that the optimal performance is achieved by setting the deposition cycles at 10 and using 4 mg of $HAuCl_4 \cdot 4H_2O$. It is worth noting that as the electrodeposition cycles and Au content increase, the OER catalytic activity of Au@NiCoFeS initially rises and then falls. This trend may be attributed to the initial distribution of Au as single atoms, where an increase in Au loading helps increase the number of active sites, thereby enhancing catalytic activity [28–30]. However, further increases in Au loading may lead to the aggregation of single atoms, resulting in the formation of nano-clusters or particles, thereby reducing catalytic activity.

Simultaneously, different noble metal single atoms were loaded to compare their OER performance. The OER catalytic activity of samples with NiCoFeS loaded with Ru, Ir, Au, and Pt was tested as working electrodes. Polarization curves are shown in Supplementary Figure S7. Compared to Pt@NiCoFeS, Ir@NiCoFeS, and Ru@NiCoFeS, Au@NiCoFeS demonstrates excellent OER activity at both low and high current densities, indicating the outstanding promotional effect of Au on OER. In addition to activity, long-term electrolysis

stability is also an important criterion for evaluating electrode material performance. As shown in Supplementary Figure S8a, the stability of the Au@NiCoFeS electrode was tested at a current density of 200 mA cm^{-2} in a 1 M KOH electrolyte, utilizing a two-electrode system with Au@NiCoFeS as the anode and nickel foam as the cathode. The results indicate that Au@NiCoFeS can operate stably for 250 h without performance degradation at a current density of 200 mA/cm^2, suggesting its significant potential for practical applications under operating conditions. By comparing the linear scan voltammetry (LSV) polarization curves before and after the stability test in Supplementary Figure S8b, it is evident that Au@NiCoFeS maintains good activity, demonstrating its excellent long-term electrolysis stability.

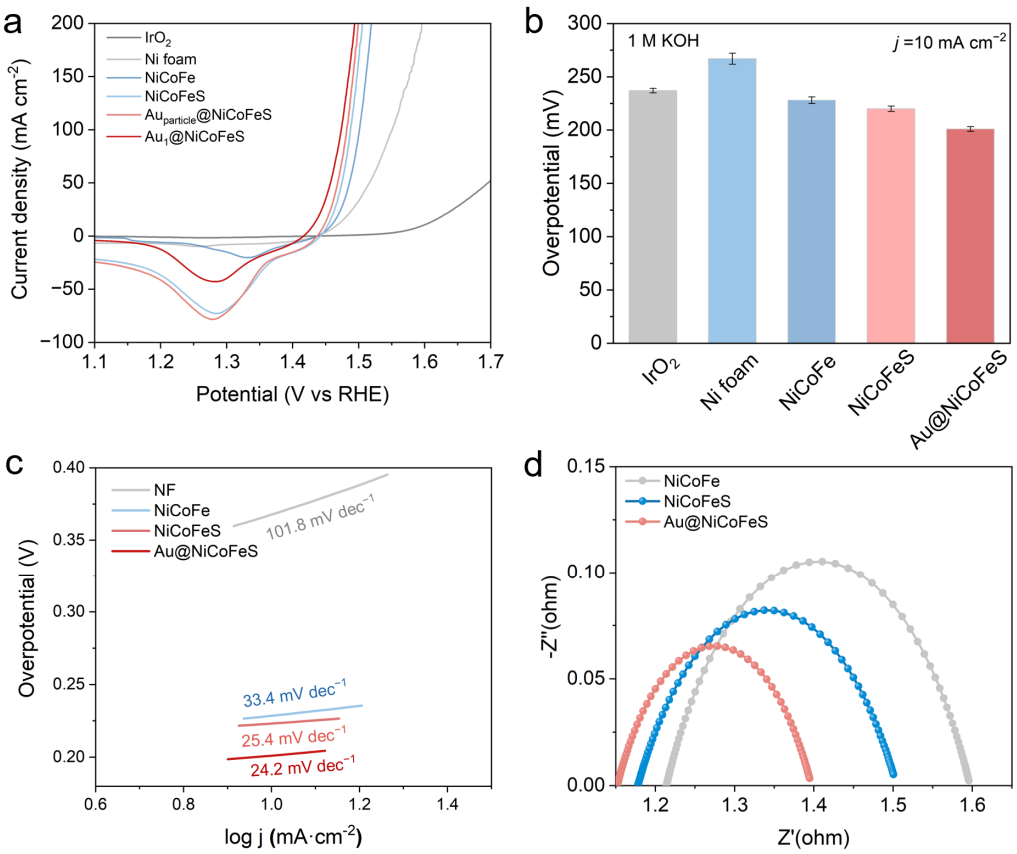

Figure 3. (**a**) Polarization curves, (**b**) corresponding overpotential at 10 mA/cm^2 (three measurements were conducted for each data point with the error bars corresponding to the standard deviation), and (**c**) Tafel slope of IrO_2, Ni foam, NiCoFe, NiCoFeS, $Au_{particle}$@NiCoFeS, and Au_1@NiCoFeS in 1 M KOH. (**d**) Nyquist plot of NiCoFe, NiCoFeS, and Au@NiCoFeS in 1 M KOH.

Furthermore, to investigate the impact of single-atom Au introduction on the number of catalytic active sites, cyclic voltammetry polarization curves were measured and fitted for Au@NiCoFeS, NiCoFeS, and NiCoFe electrodes, and the double-layer capacitance (Cdl) of the three electrodes was calculated. A larger Cdl value indicates a greater number of active sites and a larger electrochemical active surface area. Cyclic voltammetry tests were conducted on Au@NiCoFeS, NiCoFeS, and NiCoFe electrodes at scan rates of 5, 10, 15, 20, 25, and 30 mV s^{-1} within the voltage range of 0.83 V to 0.91 V vs. RHE in 1 M KOH electrolyte (Supplementary Figure S9a–c), and the Cdl values of the three electrodes were determined through curve fitting (Supplementary Figure S9d). The results demonstrate that the Cdl value of the Au@NiCoFeS electrode is 11.58 mF cm^{-2}, significantly higher than that of the NiCoFeS electrode (6.3 mF cm^{-2}) and NiCoFe (0.54 mF cm^{-2}). This indicates that the effective loading of single-atom Au enhances the electrochemical active surface area, facilitating the exposure of more active sites during the OER process.

To further assess the activity of Au@NiCoFeS in seawater electrolyte, the OER performance of the prepared samples was evaluated in alkaline seawater using a standard three-electrode system. Figure 4a demonstrates that Au@NiCoFeS achieves a current density of 10 mA/cm^2 with only 183 mV of overpotential, placing its performance in the top tier among alkaline seawater electrolysis catalysts, surpassing NiCoFeS (217 mV), NiCoFe (241 mV), and Ni foam (361 mV), and even outperforming commercial IrO_2 electrodes (241 mV), with an overpotential reduction of 58 mV (Figure 4b). Further comparison of the Tafel slope of the four electrodes (Figure 4c) reveal that the Tafel slope of the Au@NiCoFeS electrode is 25.2 mV dec^{-1}, smaller than that of NiCoFeS (27.6 mV dec^{-1}) and NiCoFe (36.8 mV dec^{-1}), indicating that the introduction of single-atom Au significantly enhances the OER kinetics of the catalyst, even in seawater electrolyte.

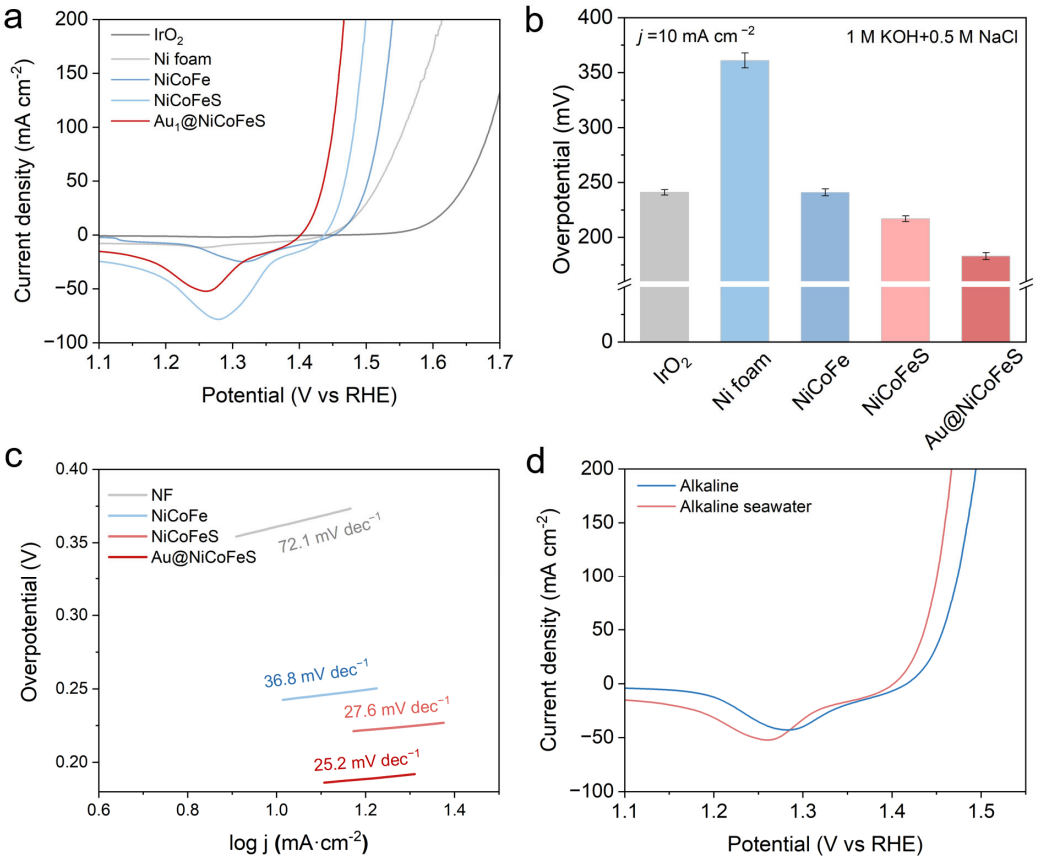

Figure 4. (**a**) Polarization curves, (**b**) corresponding overpotential at 10 mA/cm^2 (three measurements were conducted for each data point with the error bars corresponding to the standard deviation), and (**c**) Tafel slope of IrO_2, Ni foam, NiCoFe, NiCoFeS, and Au@NiCoFeS in 1 M KOH + 0.5 M NaCl. (**d**) Polarization curves of Au@NiCoFeS in alkaline electrolyte (1 M KOH) and alkaline seawater electrolyte (1 M KOH + 0.5 M NaCl).

Interestingly, the OER activity of Au@NiCoFeS in the alkaline seawater electrolyte (1 M KOH + 0.5 M NaCl) was even superior to that in the alkaline electrolyte (1 M KOH) (Figure 4d), with an overpotential reduction of 18 mV at a current density of 10 mA/cm^2. In addition, the turnover frequency (TOF) per Au site on Au@NiCoFeS at the potential of 1.45 V (versus RHE) in alkaline simulated seawater is 9.9 ± 0.5 s^{-1}, higher than that of in alkaline electrolyte (3.4 ± 0.5 s^{-1}), which further confirms that Au@NiCoFeS exhibits enhanced activity in Cl^--rich environments (see j values in Supplementary Figure S10 and details in Section 3.12 TOF calculation). However, in most cases, the activity of catalysts in seawater is significantly lower than that in alkaline electrolyte. This may be attributed to the abundant presence of Cl^- ions in seawater, which adsorb and modulate the electronic

structure and coordination state of single-atom Au, thereby enhancing the OER activity of Au@NiCoFeS in seawater [17].

In addition, the abundant presence of Cl^- in seawater can lead to competing chloride oxidation reactions at the anode, corroding the substrate and catalytic materials [31]. Therefore, the corrosion resistance and stability of the catalyst during seawater electrolysis are crucial. To investigate the stability of Au@NiCoFeS in seawater electrolyte, the OER stability of Au@NiCoFeS was tested at a current density of 200 mA/cm^2 in a 1 M KOH + 0.5 M NaCl electrolyte using a two-electrode system (Supplementary Figure S11a). The results show that Au@NiCoFeS can operate stably for 250 h in seawater electrolyte. Furthermore, the Au@NiCoFeS electrode demonstrate nearly 100% faradaic efficiency (Supplementary Figure S12) and OER selectivity during seawater splitting, showing no active chlorine (0 ppm) in the electrolyte (Supplementary Figure S13) after a chronopotentiometry (CP) test. By comparing the LSV polarization curves before and after the stability test (Supplementary Figure S11b), the two curves remain almost identical, indicating that the performance of Au@NiCoFeS does not significantly degrade after 250 h of reaction in seawater electrolyte, confirming its good long-term electrolysis activity and stability in seawater electrolyte as well. Moreover, the turnover number (TON) of Au@NiCoFeS at 0.2 A cm^{-2} in seawater was 117,600, which demonstrates the long-term stability of Au single atoms. SEM images of Au@NiCoFeS after the stability test (Supplementary Figure S14a,b) show that the original nanosheet array structure of the catalyst remains intact, and there is no significant corrosion or collapse of the catalyst and substrate. The XRD patterns of Au@NiCoFeS after the stability test (Supplementary Figure S15), which indicate no significant changes in diffraction peaks compared to initial XRD patterns, demonstrate structural stability after OER. Furthermore, TEM images of post-catalysis Au@NiCoFeS shows no discernible particles (Supplementary Figure S16), which indicates the absence of nanoparticle formation during OER. All of these characteristics indicate that Au@NiCoFeS possesses excellent water electrolysis stability and corrosion resistance, which may be attributed to the in situ formation of polysulfides during the OER process, which adsorb on the electrode surface to protect the catalyst from Cl^- attack.

3. Materials and Methods

3.1. Chemicals

Iron(III) nitrate nine-hydrate ($Fe(NO_3)_3{\cdot}9H_2O$, 99.99%), cobalt(II) nitrate hexahydrate ($Co(NO_3)_2{\cdot}6H_2O$, 99.99%), and nickel(II) nitrate hexahydrate ($Ni(NO_3)_2{\cdot}6H_2O$, 99.99%) were purchased from Sigma-Aldrich, Saint Louis, MO, USA. Potassium hydroxide (KOH, ≥96%), sodium chloride (NaCl, ≥99.5%), and sodium sulfide nonahydrate ($Na_2S{\cdot}9H_2O$) were purchased from Fuchen Chemical Reagent Co., Ltd. (Tianjin, China). Ethanol (CH_3CH_2OH, ≥99.5%) was purchased from Tianjin Fuyu Fine Chemical Co., Ltd. (Tianjin, China). Hexachloroplatinic acid hexahydrate ($H_2PtCl_6{\cdot}6H_2O$), hexachloroiridic acid hexahydrate ($H_2IrCl_6{\cdot}6H_2O$), ruthenium trichloride ($RuCl_3$), and gold chloride hydrate ($HAuCl_4{\cdot}4H_2O$) were purchased from the Shenyang Institute of Nonferrous Metals (Shenyang, China). Deionized (DI) water (resistivity: 18.3 MΩ cm) was used for the preparation of all aqueous solutions.

3.2. Pretreatment of Ni Foam

First, the 1.7 mm thick nickel foam was pretreated by cutting it into pieces of size 3 cm × 4 cm. Subsequently, the nickel foam pieces were then separately immersed in anhydrous ethanol, hydrochloric acid, acetone, and deionized water (resistivity: 18.3 MΩ cm), and subjected to ultrasonication for 10–15 min; the purpose of this step was to remove oil and oxides from the surface of the nickel foam. After cleaning, the nickel foam pieces were move into transferred to a 60 °C vacuum drying oven to remove the water, in preparation for subsequent use.

3.3. Synthesis of NiCoFe

NiCoFe was grown in situ on the nickel foam substrate via a hydrothermal method. A solution was prepared by dissolving 0.096 g of $Ni(NO_3)_2 \cdot 6H_2O$, 0.096 g of $Co(NO_3)_2 \cdot 6H_2O$, 0.13 g of $Fe(NO_3)_3 \cdot 9H_2O$, 0.60 g of $CO(NH_2)_2$, and 0.30 g of NH_4F in 36 mL of deionized water (resistivity: 18.3 MΩ cm). After ultrasonic mixing, the solution was transferred to a 50 mL high-pressure reaction vessel. Subsequently, the cleaned 3 cm × 4 cm nickel foam was placed into the high-pressure reaction vessel. The reaction vessel was then placed in a 120 °C oven and reacted for 12 h. The resulting product was washed repeatedly with deionized water and anhydrous ethanol, and then dried overnight at 60 °C to obtain NiCoFe hydroxide.

3.4. Synthesis of NiCoFeS

The prepared NiCoFe hydroxide was converted into NiCoFeS electrodes through a hydrothermal sulfidation process. First, 1.09 g of $Na_2S \cdot 9H_2O$ was dissolved in 36 mL of deionized water, and the solution was ultrasonically mixed. Then, the solution was transferred to a 50 mL high-pressure reaction vessel. Subsequently, the prepared 3 cm × 4 cm NiCoFe hydroxide was transferred to the high-pressure reaction vessel. The reaction vessel was then placed in an oven at 120 °C and allowed to react for 4 h. After the reaction, the resulting product was washed repeatedly with deionized water and anhydrous ethanol. Finally, the product was dried overnight at 60 °C to obtain NiCoFeS electrodes.

3.5. Synthesis of Au@NiCoFeS

To prepare Au@NiCoFeS, an electrodeposition method was employed [32]. Firstly, the prepared NiCoFeS was cut into pieces of size 1 cm × 2 cm. A standard three-electrode system was set up with NiCoFeS as the working electrode, a carbon rod as the counter electrode, and a saturated calomel electrode (SCE) as the reference electrode; a 100 μmol/L $HAuCl_4$ solution dissolved in 1 M KOH served as the electrolyte. Electrodeposition was carried out within the potential range of −0.97 V to −1.47 V vs. SCE at a scan rate of 5 mV/s for 10 cycles. After deposition, the samples were washed repeatedly with deionized water and anhydrous ethanol, and then dried in a 60 °C oven for 4 h to obtain Au single-atom-loaded NiCoFeS nanoarray electrodes (Au@NiCoFeS).

3.6. Synthesis of Ir@NiCoFeS

To prepare Ir@NiCoFeS, an electrodeposition method was employed. Initially, the prepared NiCoFeS was cut into pieces of size 1 cm × 2 cm. Subsequently, a standard three-electrode system was established with NiCoFeS serving as the working electrode, a carbon rod as the counter electrode, and a saturated calomel electrode (SCE) as the reference electrode. Solutions of 100 μmol/L H_2IrCl_6 dissolved in 1 M KOH were configured as the electrolytes for Ir deposition. Electrodeposition was conducted within the potential range of −0.97 V to −1.47 V vs. SCE, with a scan rate of 5 mV/s for 10 cycles. After deposition, the deposited samples underwent repeated washing with deionized water and anhydrous ethanol. Subsequently, the samples were dried in a 60 °C oven for 4 h to obtain Ir single-atom-loaded NiCoFeS nanoarray electrodes (Ir@NiCoFeS).

3.7. Synthesis of Pt@NiCoFeS

To prepare Pt@NiCoFeS, an electrodeposition method was employed. Initially, the prepared NiCoFeS was cut into pieces of size 1 cm × 2 cm. Subsequently, a standard three-electrode system was established with NiCoFeS serving as the working electrode, a carbon rod as the counter electrode, and a saturated calomel electrode (SCE) as the reference electrode. Solutions of 100 μmol/L H_2PtCl_6 dissolved in 1 M KOH were configured as the electrolytes for Pt deposition. Electrodeposition was conducted within the potential range of −0.97 V to −1.47 V vs. SCE, with a scan rate of 5 mV/s for 10 cycles. After deposition, the deposited samples underwent repeated washing with deionized water and

anhydrous ethanol. Subsequently, the samples were dried in a 60 °C oven for 4 h to obtain Pt single-atom-loaded NiCoFeS nanoarray electrodes (Pt@NiCoFeS).

3.8. Synthesis of Ru@NiCoFeS

To prepare Ru@NiCoFeS, an electrodeposition method was employed. Initially, the prepared NiCoFeS was cut into pieces of size 1 cm × 2 cm. Subsequently, a standard three-electrode system was established with NiCoFeS serving as the working electrode, a carbon rod as the counter electrode, and a saturated calomel electrode (SCE) as the reference electrode. Solutions of 100 μmol/L $RuCl_3$ dissolved in 1 M KOH were configured as the electrolytes for Ru deposition. Electrodeposition was conducted within the potential range of −0.97 V to −1.47 V vs. SCE, with a scan rate of 5 mV/s for 10 cycles. After deposition, the deposited samples underwent repeated washing with deionized water and anhydrous ethanol. Subsequently, the samples were dried in a 60 °C oven for 4 h to obtain Ru single-atom-loaded NiCoFeS nanoarray electrodes (Ru@NiCoFeS).

3.9. HAADF-STEM Characterization

Before imaging, the as-prepared Au@NiCoFeS catalysts were added into anhydrous ethanol by using an ultrasonator to form a very dilute colloid suspension; then, the 20 μL suspension was dripped onto 230-mesh Cu grids coated with ultrathin carbon. The high-resolution HAADF-STEM image was acquired using a Thermo Fisher (Waltham, MA, USA) Spectra 300 microscope equipped with an aberration corrector for the probe-forming lens, operated at 300 kV. The beam current was lower than 40 pA and the STEM convergence semi-angle was ~25 mrad, which provided a probe size of ~0.6 Å at 300 kV.

3.10. Material Characterization

Scanning electron microscope (SEM) measurement was carried out on a Zeiss Supra 55 operated at 20 kV. Transmission electron microscopy (TEM) measurement was carried out on a JEOL (Peabody, MA, USA) JEM 2100. X-ray powder diffraction (XRD) patterns were recorded on an X-ray diffractometer (Rigaku D/max 2500) with Cu Kα radiation (40 kV, 30 mA, λ = 1.5418 Å) at a scan rate of 5° min^{-1} in the 2θ range from 3 to 90°. X-ray photoelectron spectroscopy (XPS) spectra were recorded on an ESCALAB 250 (Thermo Fisher Scientific, USA) photoelectron spectrometer using a monochromate Al Kα 150 W X-ray beam. All binding energies were referenced to the C 1 s peak (284.8 eV). Specifically, by evaluating the deviation of the binding energy position corresponding to the C 1 s peak at 284.8 eV, the obtained difference was then utilized to carry out a comprehensive calibration of the entire dataset. All data were acquired without background subtraction to ensure the accuracy of peak fitting. A Gaussian–Lorentzian fitting curve was employed, and analysis was conducted using the Avantage software (Version 5.99311).

3.11. Electrochemical Measurements

All the electrocatalytic experiments were performed on a typical three-electrode system (the three-electrode cell was purchased from Tianjin Aida Hengsheng Technology Development Co., Ltd., Tianjin, China) using a CHI 660e electrochemical workstation (CH Instruments, Inc., Shanghai, China). All of the as-prepared catalysts were used as working electrodes. A carbon rod electrode and a saturated calomel electrode (SCE) were used as counter and reference electrodes, respectively (the saturated calomel electrode (SCE), which was purchased from Tianjin Aida Hengsheng Technology Development Co., Ltd., consists of saturated KCl). The working surface area of the electrode was 1 cm^2, and the volume of the electrolyte was 200 mL. The stability test was conducted using a standard two-electrode system, with Au@NiCoFeS employed as the anode and Ni foam as the cathode. The stability test was performed separately in 1 M KOH and 1 M KOH + 0.5 M NaCl electrolytes at 0.2 A/cm^2. All measured potentials vs. SCE were converted to a reversible hydrogen electrode (RHE) according to the Nernst equation ($E_{(RHE)} = E_{(SCE)} + 0.059\ pH + 0.244$ V). Polarization curves were obtained using cycling voltammetry (CV) at the range from 0 to

1.0 V versus SCE with a scan rate of 5 mV s^{-1}. Electrochemical impedance spectroscopy (EIS) was measured by applying an AC voltage of 5 mV at the overpotential of 10 mV with a frequency from 1000 kHz to 0.1 Hz. All polarization curves were corrected for Ohmic-drop compensation with Ohmic resistance obtained by the EIS. The faradaic efficiency was calculated using the formula Faradaic efficiency $(\%) = \frac{\text{Actual moles of oxygen produced}}{\text{Theoretical oxygen evolution moles}} \times 100\%$, and the oxygen generated at the anode was collected by the water displacement method. A H cell was utilized as the electrochemical cell, with Au@NiCoFeS utilized as the working electrode; a carbon rod electrode and a saturated calomel electrode (SCE) were used as counter and reference electrodes, respectively. An anion exchange membrane (AEM) was utilized to facilitate OH- conduction while preventing the mixing of hydrogen and oxygen. Chronopotentiometry (CP) tests were conducted at 0.2 A/cm^2 in 1 M KOH + 0.5 M NaCl, and the gas generated at the anode was collected in an inverted burette filled with water, and the volume of evolved oxygen was determined based on the electrolysis time.

3.12. Turnover Frequency (TOF) Calculation

The turnover frequency (TOF) per Au site was calculated according to the following equation:

$$\text{TOF } (O_2/s) = \frac{\text{oxygen turnover per geometric area}}{\text{number of active Au sites per geometric area}}$$

The number of oxygen turnovers could be obtained by current density using the following formula:

Number of oxygen turnovers:

$$= \left(|j| \text{ mA cm}^{-2}\right)\left(\frac{1C}{1000 \text{ mA·s}}\right)\left(\frac{1 \text{ mol } e^-}{96{,}485.3 \text{ C}}\right)\left(\frac{1 \text{ mol } O_2}{4 \text{ mol } e^-}\right)\left(\frac{6.022 \times 10^{23} \text{ molecules } O_2}{1 \text{ mol } O_2}\right)$$
$$= 1.560 \times 10^{15} \text{ } |j| \text{ cm}^{-2}s^{-1}b$$

The number of Au active sites in Au@NiCoFeS was calculated according to the mass loading of Au on the electrode (dispersed Au atoms were anchored on the surface of NiCoFeS, which acted as the active sites to catalyze the oxygen evolution reaction):

Number of Au active sites:

$$= \left(\frac{\text{catalyst loading per geometric area} \times \text{Au wt.\%}}{\text{Au Mw}}\right) \times \left(\frac{6.022 \times 10^{23} \text{ Au atoms}}{1 \text{ mol Au}}\right)$$
$$= \left(\frac{1 \text{ mg cm}^{-2} \times 0.52 \text{ wt.\%}}{196.97 \text{ g mol}^{-1}}\right) \times \left(\frac{6.022 \times 10^{23} \text{ Au atoms}}{1 \text{ mol Au}}\right) = 1.589 \times 10^{16} \text{cm}^{-2}$$

So, TOF can be calculated:

$$\text{TOF} = \frac{1.560 \times 10^{15} \text{ cm}^{-2}s^{-1}}{1.589 \times 10^{16} \text{ cm}^{-2}} \times |j| = 0.098 \times |j| \text{ s}^{-1}$$

3.13. Turnover Number (TON) Calculation

$$\text{TON} = \text{TOF} \times \text{reaction time}\left(\text{the time when Faradaic efficiency equal to 100\%, j} = 0.2 \text{ A/cm}^2\right)$$
$$= \frac{\text{oxygen turnover per geometric area}}{\text{number of active Au sites per geometric area}} \times \text{reaction time}$$
$$= 0.098 \times |j| \text{ s}^{-1} \times 100 \times 60 \text{ s} = 117{,}600$$

4. Conclusions

This study employs the electrodeposition method to load single-atom Au onto NiCoFeS substrates for seawater electrolysis oxygen evolution reactions. The Au@NiCoFeS catalyst exhibits remarkable OER activity and stability in both alkaline and seawater electrolytes. High-angle annular dark-field scanning transmission electron microscopy (HAADF-STEM) confirms the uniform dispersion of Au on the NiCoFeS surface. In contrast to conventional seawater electrolysis catalysts experiencing performance degradation in seawater environments, Au@NiCoFeS exhibits superior catalytic activity in alkaline seawater electrolyte

compared to alkaline electrolyte, requiring only 183 mV to achieve a current density of 10 mA/cm^2. It ranks among the top-tier anode catalysts for alkaline seawater electrolysis. Furthermore, it can operate at a current density of 200 mA/cm^2 for 250 h without corrosion or decay in alkaline seawater electrolyte, showcasing excellent industrial applicability. This research expands the utilization of easily synthesized single-atom catalysts in electrochemical seawater oxidation, offering promising prospects for further advancements in this field.

Supplementary Materials: The following supporting information can be downloaded at https://www.mdpi.com/article/10.3390/catal14060348/s1: Supplementary Figure S1: SEM images of (a) Ni foam, (b) NiCoFeS. Supplementary Figure S2: EDS mapping of Au@NiCoFeS. Supplementary Figure S3: Low-magnified TEM image of Au@NiCoFeS. Supplementary Figure S4: XRD patterns of NiCoFeS and Au@NiCoFeS. Supplementary Figure S5: High-resolution XPS spectra of S 2p of Au@NiCoFeS. Supplementary Figure S6: (a) Polarization curves of Au@NiCoFeS with different electrodeposition cycles in 1 M KOH. (b) Polarization curves of Au@NiCoFeS with different Au mass loading in 1 M KOH. Supplementary Figure S7: Polarization curves of Ru@NiCoFeS, Ir@NiCoFeS, Au@NiCoFeS, and Pt@NiCoFeS in 1 M KOH. Supplementary Figure S8: (a) Chronopotentiometry curves of Au@NiCoFeS at 200 mA/cm^2 in 1 M KOH. (b) Polarization curves of Au@NiCoFeS before and after stability test in 1 M KOH. Supplementary Figure S9: The polarization curves of (a) NiCoFe, (b) NiCoFeS, and (c) Au@NiCoFeS in 1 M KOH. (d) C_{dl} of NiCoFe, NiCoFeS, and Au@NiCoFeS. Supplementary Figure S10: The j value of Au@NiCoFeS at 1.45 V vs RHE in 1 M KOH + 0.5 M NaCl and 1 M KOH. Three measurements were conducted for each data point with the error bars corresponding to the standard deviation. Supplementary Figure S11: (a) Chronopotentiometry curves of Au@NiCoFeS at 200 mA/cm^2 in 1 M KOH + 0.5 M NaCl. (b) Polarization curves of Au@NiCoFeS before and after stability test in 1 M KOH + 0.5 M NaCl. Supplementary Figure S12: The mole amount of oxygen evolved (red dots), the theoretical oxygen evolution value (blue dashed line), and the faradaic efficiency (brown squares) of Au@NiCoFeS. Theoretical oxygen evolution value was calculated based on the number of consumed charges over the electrolysis. Supplementary Figure S13: Active chlorine test of 1 M NaOH + 0.5 M NaCl electrolyte after chronopotentiometry (CP) test at 0.2 A/cm^2. Supplementary Figure S14: (a) Low-magnified and (b) high-magnified SEM images of Au@NiCoFeS after stability test in 1 M KOH+0.5 M NaCl. Supplementary Figure S15: XRD patterns of Au@NiCoFeS after stability test. Supplementary Figure S16: TEM image of Au@NiCoFeS after stability test.

Author Contributions: Writing—original draft, Q.S.; writing—review & editing, Q.S.; formal analysis, Q.S., J.S., G.Y. and T.L.; investigation, J.S. and G.Y.; validation, W.L.; resources, Y.K. and X.S.; project administration, Y.K. and X.S.; funding acquisition, Y.K. and X.S. All authors have read and agreed to the published version of the manuscript.

Funding: This work was supported by the Science and Technology Innovation Foundation of Laoshan Laboratory (No. LSKJ202205700), the Xinjiang Uygur Autonomous Region Key R&D Projects (No. 202114958) and Shenzhen Energy Group Co., Ltd. The authors also thanks for National Key R&D Program of China (2021YFA1502200), the National Natural Science Foundation of China, the Key Research Project of Beijing Natural Science Foundation.

Data Availability Statement: The data that support the findings of this study have been included in the main text and Supplementary Information. All other relevant data supporting the findings of this study are available from the corresponding authors upon request.

Conflicts of Interest: The authors declare that this study received funding from Shenzhen Energy Group Co., Ltd. The funder was not involved in the study design, collection, analysis, interpretation of data, the writing of this article or the decision to submit it for publication.

References

1. Xie, H.; Zhao, Z.; Liu, T.; Wu, Y.; Lan, C.; Jiang, W.; Zhu, L.; Wang, Y.; Yang, D.; Shao, Z. A membrane-based seawater electrolyser for hydrogen generation. *Nature* **2022**, *612*, 673–678. [CrossRef] [PubMed]
2. Kuang, Y.; Kenney, M.J.; Meng, Y.; Hung, W.-H.; Liu, Y.; Huang, J.E.; Prasanna, R.; Li, P.; Li, Y.; Wang, L.; et al. Solar-driven, highly sustained splitting of seawater into hydrogen and oxygen fuels. *Proc. Natl. Acad. Sci. USA* **2019**, *116*, 6624–6629. [CrossRef]

3. Dresp, S.; Dionigi, F.; Klingenhof, M.; Strasser, P. Direct Electrolytic Splitting of Seawater: Opportunities and Challenges. *ACS Energy Lett.* **2019**, *4*, 933–942. [CrossRef]
4. Bednar, J.; Obersteiner, M.; Baklanov, A.; Thomson, M.; Wagner, F.; Geden, O.; Allen, M.; Hall, J.W. Operationalizing the net-negative carbon economy. *Nature* **2021**, *596*, 377–383. [CrossRef]
5. Tong, D.; Zhang, Q.; Zheng, Y.; Caldeira, K.; Shearer, C.; Hong, C.; Qin, Y.; Davis, S.J. Committed emissions from existing energy infrastructure jeopardize 1.5 °C climate target. *Nature* **2019**, *572*, 373–377. [CrossRef]
6. Hu, H.; Wang, X.; Attfield, J.P.; Yang, M. Metal nitrides for seawater electrolysis. *Chem. Soc. Rev.* **2024**, *53*, 163–203. [CrossRef]
7. Wang, Y.; Wang, M.; Yang, Y.; Kong, D.; Meng, C.; Zhang, D.; Hu, H.; Wu, M. Potential technology for seawater electrolysis: Anion-exchange membrane water electrolysis. *Chem Catal.* **2023**, *3*, 100643. [CrossRef]
8. Liu, X.; Chi, J.; Mao, H.; Wang, L. Principles of Designing Electrocatalyst to Boost Reactivity for Seawater Splitting. *Adv. Energy Mater.* **2023**, *13*, 2301438. [CrossRef]
9. Yu, Z.-Y.; Duan, Y.; Feng, X.-Y.; Yu, X.; Gao, M.-R.; Yu, S.-H. Clean and Affordable Hydrogen Fuel from Alkaline Water Splitting: Past, Recent Progress, and Future Prospects. *Adv. Mater.* **2021**, *33*, 2007100. [CrossRef]
10. Liu, J.; Duan, S.; Shi, H.; Wang, T.; Yang, X.; Huang, Y.; Wu, G.; Li, Q. Rationally Designing Efficient Electrocatalysts for Direct Seawater Splitting: Challenges, Achievements, and Promises. *Angew. Chem. Int. Ed.* **2022**, *61*, e202210753. [CrossRef]
11. Guo, J.; Zheng, Y.; Hu, Z.; Zheng, C.; Mao, J.; Du, K.; Jaroniec, M.; Qiao, S.-Z.; Ling, T. Direct seawater electrolysis by adjusting the local reaction environment of a catalyst. *Nat. Energy* **2023**, *8*, 264–272. [CrossRef]
12. Li, T.; Zhao, X.; Getaye Sendeku, M.; Zhang, X.; Xu, L.; Wang, Z.; Wang, S.; Duan, X.; Liu, H.; Liu, W.; et al. Phosphate-decorated Ni3Fe-LDHs@CoPx nanoarray for near-neutral seawater splitting. *Chem. Eng. J.* **2023**, *460*, 141413. [CrossRef]
13. Ma, T.; Xu, W.; Li, B.; Chen, X.; Zhao, J.; Wan, S.; Jiang, K.; Zhang, S.; Wang, Z.; Tian, Z.; et al. The Critical Role of Additive Sulfate for Stable Alkaline Seawater Oxidation on Nickel-Based Electrodes. *Angew. Chem. Int. Ed.* **2021**, *60*, 22740–22744. [CrossRef] [PubMed]
14. Yu, L.; Wu, L.; McElhenny, B.; Song, S.; Luo, D.; Zhang, F.; Yu, Y.; Chen, S.; Ren, Z. Ultrafast room-temperature synthesis of porous S-doped Ni/Fe (oxy)hydroxide electrodes for oxygen evolution catalysis in seawater splitting. *Energy Environ. Sci.* **2020**, *13*, 3439–3446. [CrossRef]
15. Zhao, Y.; Jin, B.; Zheng, Y.; Jin, H.; Jiao, Y.; Qiao, S.-Z. Charge State Manipulation of Cobalt Selenide Catalyst for Overall Seawater Electrolysis. *Adv. Energy Mater.* **2018**, *8*, 1801926. [CrossRef]
16. Yu, L.; Zhu, Q.; Song, S.; McElhenny, B.; Wang, D.; Wu, C.; Qin, Z.; Bao, J.; Yu, Y.; Chen, S.; et al. Non-noble metal-nitride based electrocatalysts for high-performance alkaline seawater electrolysis. *Nat. Commun.* **2019**, *10*, 5106. [CrossRef]
17. Duan, X.; Sha, Q.; Li, P.; Li, T.; Yang, G.; Liu, W.; Yu, E.; Zhou, D.; Fang, J.; Chen, W.; et al. Dynamic chloride ion adsorption on single iridium atom boosts seawater oxidation catalysis. *Nat. Commun.* **2024**, *15*, 1973. [CrossRef] [PubMed]
18. Huang, C.; Zhou, Q.; Duan, D.; Yu, L.; Zhang, W.; Wang, Z.; Liu, J.; Peng, B.; An, P.; Zhang, J.; et al. The rapid self-reconstruction of Fe-modified Ni hydroxysulfide for efficient and stable large-current-density water/seawater oxidation. *Energy Environ. Sci.* **2022**, *15*, 4647–4658. [CrossRef]
19. Zhuang, L.; Li, J.; Wang, K.; Li, Z.; Zhu, M.; Xu, Z. Structural Buffer Engineering on Metal Oxide for Long-Term Stable Seawater Splitting. *Adv. Funct. Mater.* **2022**, *32*, 2201127. [CrossRef]
20. Dresp, S.; Ngo Thanh, T.; Klingenhof, M.; Brückner, S.; Hauke, P.; Strasser, P. Efficient direct seawater electrolysers using selective alkaline NiFe-LDH as OER catalyst in asymmetric electrolyte feeds. *Energy Environ. Sci.* **2020**, *13*, 1725–1729. [CrossRef]
21. Shi, Z.; Wang, Y.; Li, J.; Wang, X.; Wang, Y.; Li, Y.; Xu, W.; Jiang, Z.; Liu, C.; Xing, W. Confined Ir single sites with triggered lattice oxygen redox: Toward boosted and sustained water oxidation catalysis. *Joule* **2021**, *5*, 2164–2176. [CrossRef]
22. Han, Z.-K.; Sarker, D.; Ouyang, R.; Mazheika, A.; Gao, Y.; Levchenko, S.V. Single-atom alloy catalysts designed by first-principles calculations and artificial intelligence. *Nat. Commun.* **2021**, *12*, 1833. [CrossRef] [PubMed]
23. Chen, C.-H.; Wu, D.; Li, Z.; Zhang, R.; Kuai, C.-G.; Zhao, X.-R.; Dong, C.-K.; Qiao, S.-Z.; Liu, H.; Du, X.-W. Ruthenium-Based Single-Atom Alloy with High Electrocatalytic Activity for Hydrogen Evolution. *Adv. Energy Mater.* **2019**, *9*, 1803913. [CrossRef]
24. Zhang, L.; Han, L.; Liu, H.; Liu, X.; Luo, J. Potential-Cycling Synthesis of Single Platinum Atoms for Efficient Hydrogen Evolution in Neutral Media. *Angew. Chem. Int. Ed.* **2017**, *56*, 13694–13698. [CrossRef] [PubMed]
25. Li, P.; Wang, M.; Duan, X.; Zheng, L.; Cheng, X.; Zhang, Y.; Kuang, Y.; Li, Y.; Ma, Q.; Feng, Z.; et al. Boosting oxygen evolution of single-atomic ruthenium through electronic coupling with cobalt-iron layered double hydroxides. *Nat. Commun.* **2019**, *10*, 1711. [CrossRef] [PubMed]
26. Li, M.; Xie, P.; Yu, P.; Luo, P.; Sun, X. Bubble Engineering on Micro-/Nanostructured Electrodes for Water Splitting. *ACS Nano* **2023**, *17*, 23299–23316. [CrossRef] [PubMed]
27. Zhang, J.; Liu, J.; Xi, L.; Yu, Y.; Chen, N.; Sun, S.; Wang, W.; Lange, K.M.; Zhang, B. Single-Atom Au/NiFe Layered Double Hydroxide Electrocatalyst: Probing the Origin of Activity for Oxygen Evolution Reaction. *J. Am. Chem. Soc.* **2018**, *140*, 3876–3879. [CrossRef] [PubMed]
28. Wang, A.; Li, J.; Zhang, T. Heterogeneous single-atom catalysis. *Nat. Rev. Chem.* **2018**, *2*, 65–81. [CrossRef]
29. Qiao, B.; Wang, A.; Yang, X.; Allard, L.F.; Jiang, Z.; Cui, Y.; Liu, J.; Li, J.; Zhang, T. Single-atom catalysis of CO oxidation using Pt1/FeOx. *Nat. Chem.* **2011**, *3*, 634–641. [CrossRef]
30. Cao, L.; Liu, W.; Luo, Q.; Yin, R.; Wang, B.; Weissenrieder, J.; Soldemo, M.; Yan, H.; Lin, Y.; Sun, Z.; et al. Atomically dispersed iron hydroxide anchored on Pt for preferential oxidation of CO in H2. *Nature* **2019**, *565*, 631–635. [CrossRef]

31. Li, P.; Wang, S.; Samo, I.A.; Zhang, X.; Wang, Z.; Wang, C.; Li, Y.; Du, Y.; Zhong, Y.; Cheng, C.; et al. Common-Ion Effect Triggered Highly Sustained Seawater Electrolysis with Additional NaCl Production. *Research* **2020**, *2020*, 2872141. [CrossRef] [PubMed]
32. Zhang, Z.; Feng, C.; Liu, C.; Zuo, M.; Qin, L.; Yan, X.; Xing, Y.; Li, H.; Si, R.; Zhou, S.; et al. Electrochemical deposition as a universal route for fabricating single-atom catalysts. *Nat. Commun.* **2020**, *11*, 1215. [CrossRef] [PubMed]